

Hybrid-Order Topological Phase And Transition in 1H Transition Metal Compounds

Ning-Jing Yang,^{1,2} Zhigao Huang,^{1,2} and Jian-Min Zhang^{*1,2, a)}

¹⁾ Fujian Provincial Key Laboratory of Quantum Manipulation and New Energy Materials, College of Physics and Energy, Fujian Normal University, Fuzhou 350117, China

²⁾ Fujian Provincial Collaborative Innovation Center for Advanced High-Field Superconducting Materials and Engineering, Fuzhou, 350117, China

Inspired by recent experimental observations of hybrid topological states [Nature 628, 527 (2024)], we predict hybrid-order topological insulators (HOTIs) in 1H transition metal compounds (TMCs), where both second-order and first-order topological states coexist near the Fermi level. Initially, 1H-TMCs exhibit a second-order topological phase due to the *d*-orbital band gap. Upon coupling of *p*- and *d*-orbitals couple, first-order topological characteristics emerge. This hybrid-order topological phase transition is tunable via crystal field effects. Combined with first-principles calculations, we illustrate the phase transition with *WTe*₂ and *NbSe*₂. In addition, the first-order topological band gap of the HOTI exhibits a strong spin Hall effect. Our finding reveal novel hybrid-order topological phase in 2D electron materials and highlight spintronic applications.

Recently, Shafayat *et al.* discussed the existence of hybrid topological quantum states in solid *As* in experiment¹. By stacking *As*, they observed the co-existence of first-order topological surface and second-order hinge states. Hybrid-order topological states initially emerged in phononic crystals^{2,3}, resulting in dipole and quadrupole moments in different frequency bands. Unlike the bulk-edge correspondence in traditional topological systems⁴⁻⁷, hybrid-order topological materials exhibit novel correspondences, manifesting as a bulk-surface-edge correspondence in three-dimensional (3D) systems and as a bulk-edge-corner correspondence in two-dimensional (2D) systems^{3,8}.

However, the bulk-edge-corner correspondence has not yet been explored in 2D electronic materials. While first-order and higher-order topological materials are quite common, HOTIs have only been observed in *As*, *M₂Te₂P* and *1T'-MoTe₂* in electronic systems so far^{1,9,10}. 2D materials offer better tunability and more degrees of freedom compared to 3D materials¹¹⁻¹⁸, which suggests that they exhibit richer physical properties than 3D materials¹⁹⁻²⁸. Additionally, our current understanding of hybrid-order topological phases is limited. Therefore, it is very likely that this new type of hybrid-order topological phase is also prevalent in existing 2D materials, possibly even in the most common materials or systems we know^{10,29}. Among the most extensively discussed 2D materials are transition metal compounds (TMCs), which have shown rich physical properties in the fields of superconductivity³⁰⁻³⁴, valley physics^{35,36}, excitonics³⁷⁻³⁹, spintronics⁴⁰⁻⁴², and topology^{43,44}. The high-order topological properties of these materials have only been discovered recently^{43,44}, highlighting the great physical potential of 2D TMCs.

In this letter, we identify the hidden hybrid-order topological states in 1H-phase TMCs and elucidate the phase transition process. Firstly, we emphasize the second-order topological properties of transition metal com-

pounds 1H-*MX*₂ using the multi-orbital tight-binding (TB) model, which manifests above the Fermi level. Secondly, a first-order topological phase transition can be achieved below the Fermi level by tuning the relative energy levels between the orbitals. The phase transition process of the entire system involves the conversion between a hybrid-order topological state and a second-order topological state. These topological states are contributed by the *p* and *d* orbitals. Finally, we validate the hybrid-order phase transition process in 1H-*MX*₂ under a strain field using *NbSe*₂ and *WTe*₂ as examples in metals and semiconductors. The hybrid-order topological states that switch between first-order and second-order topology near the Fermi level break the conventional limitations of topological materials. Our results highlight the hybrid-order topological states in 2D systems and discuss the essential nature dominated by orbitals, providing a new approach for further exploration of more hybrid-order quantum materials.

The crystal structure of 1H-phase TMCs is shown in Fig. 1 (a). In the structural diagram, the blue atoms represent transition metal atoms, while green atoms typically belong to elements from the VIA groups. This 1H TMC monolayer exhibits the characteristic hexagonal lattice. We take *NbSe*₂ as an example to discuss their common physical properties. The crystal structure of 1H-*NbSe*₂ belongs to the P-6m2 space group, with its side view depicted in Fig. 1 (a).

For 1H-phase TMCs, the vicinity of the Fermi level is typically contributed by the *d* orbitals of the transition metal and the *p* orbitals of the coordinating elements. Common coordinating elements often come from the oxygen group. The stability of the crystal structure of these TMCs is closely related to the electronic distribution in the *d* orbitals and the orbital splitting in different crystal fields⁴⁵⁻⁴⁷. Taking 1H-*NbSe*₂ as an example. In this compound, the transition metal atom *Nb* forms bonds with six *Se* atoms, resulting in a trigonal prismatic crystal structure, as shown in Fig. 1 (a). Under the trigonal prismatic crystal field effect, *d* orbitals of *Nb* split into three energy levels: *d*_{3z²-r², *d*_{xy}/*d*_{x²-y², and *d*_{xz}/*d*_{yz}. The *d*_{3z²-r² orbital occupies a relatively lower energy}}}

^{a)} Corresponding author: jmzhang@fjnu.edu.cn

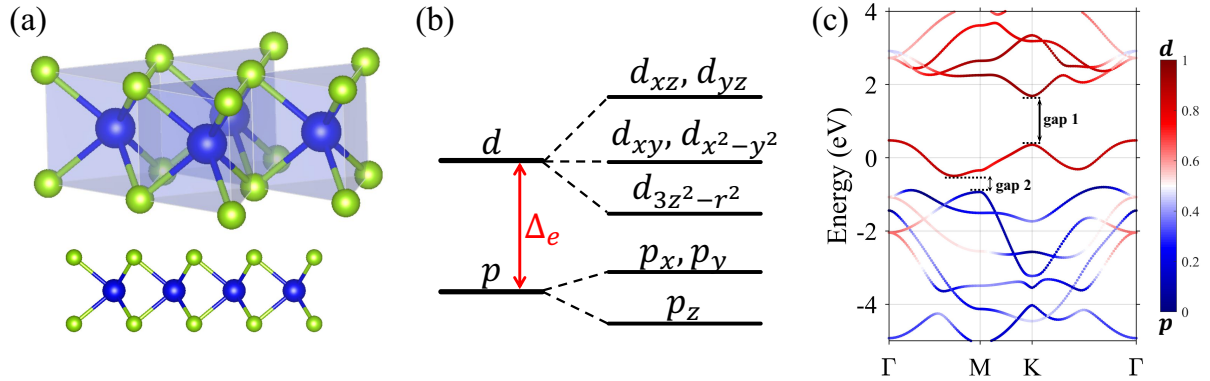


FIG. 1. (a) Crystal structure diagram of 1H TMC. (b) A schematic diagram of the energy levels occupied by p and d orbitals in the system. (c) Orbital projected band structure of $NbSe_2$ without considering SOC.

level, while $d_{xy}/d_{x^2-y^2}$ is slightly higher. The two degenerate d_{xz} and d_{yz} orbitals occupy even higher energy regions. Below these d orbitals, the p orbitals of the Se atoms split into p_z and p_x/p_y energy levels, with p_z being the lowest. The distribution of p and d orbital energy levels in the system is illustrated in Fig. 1 (b). Additionally, first-principles calculations of the projected orbital density for 1H- $NbSe_2$ confirm the localized energy distribution, as shown in Fig. S1⁴⁸. The details and discussion of the first-principles calculation parameters can be found in the supplementary materials⁴⁸.

Density functional theory calculations show the orbital projected band structure of $NbSe_2$ in Fig. 1 (c). Since spin-orbit coupling (SOC) is not considered, the spin of the energy bands does not exhibit splitting. Unlike traditional transition metal dichalcogenides (TMDs) such as MoS_2 exhibit metallic behavior due to the d orbital bands crossing the Fermi level. From the projected p , d orbital bands, we observe that d orbitals dominate the region above the Fermi level, while below the Fermi level, p orbitals play a significant role. Notably, there is strong coupling between the p and d orbitals, and a clear orbital alternation occurs at the Γ point, which has been overlooked in previous studies. The band structure reveals a relatively large gap (gap 1) between the d orbitals, and a smaller gap (gap 2) exists between the p and d orbitals. The coupling associated with the gap 2 between p and d orbitals has been neglected, emphasizing the need to reevaluate the orbital interactions near the Fermi level. We focus on the topological properties of the two direct gaps, gap 1 and gap 2, as shown in Fig. 1 (c). In the following discussion, we analyze the hidden physical correlations and topological properties using the tight-binding approximation.

The coupling between orbitals and variations in relative energy levels can be induced through adjustable crystal fields. TMCs are sensitive to stress fields. In previous studies, the focus was often limited to the physical properties of gap 1, and for simplicity, only the d orbitals were considered, neglecting the role of p orbitals. This led to the oversight of topological properties occurring in

the gap 2 interval. We will employ a second quantization methods to derive the system's Hamiltonian. This tight-binding model encompasses 5 d orbitals and $2 \cdot 3$ p orbitals, where 2 represents the Se atoms in the upper and lower layers, collectively constructing an 11-orbital tight-binding system for 1H-TMCs. The hoppings in this system are considered only between nearest neighbors. For TMC materials, which often exhibit strong spin-orbit coupling effects, the inclusion of the SOC term in the Hamiltonian is necessary. Therefore, the Hamiltonian for this system can be expressed as:

$$H = \sum_{i,\alpha} E_i^\alpha c_i^\dagger c_i + \sum_{i,j,\alpha,\beta} (t_{ij}^{\alpha,\beta} c_{i\alpha}^\dagger c_{j\beta} + h.c.) + \lambda_{soc} \mathbf{L} \cdot \mathbf{S}, \quad (1)$$

where $c_{i\alpha}^\dagger$ ($c_{j\beta}$) represents the electron creation (annihilation) operator for the orbital α (β) located at position i (j). E_i represents the onsite energy. S represents the Pauli matrix. λ_{soc} denotes the strength of the spin-orbit coupling. Detailed parameters can be found in the supplementary materials.⁴⁸

To verify the second-order topological insulator (SOTI) of 1H-TMCs, we first calculate the higher order topological indices $Q_c^{(3)}$ of the system, which is protected by the symmetry of the C_3 rotation symmetry. For calculating the rotation eigenvalues of all occupied states at the high symmetry points in the Brillouin zone, one can take $[K_n^{(3)}] = \#K_n^{(3)} - \#\Gamma_n^{(3)}$, where $\#$ denotes the counting about the symmetry eigenvalues at the points K and Γ . The topological indices^{49,50} of the HOTI are

$$\chi^{(3)} = ([K_1^{(3)}], [K_2^{(3)}]), Q_c^{(3)} = \frac{e}{3} [K_2^{(3)}] \bmod e, \quad (2)$$

where e is the charge of the free electron. The upper indicator (3) represents C_3 symmetry. Then, the topological indicator $\chi^{(3)} = (1, 2)$ and the nonzero corner charge $Q_c^{(3)} = 2e/3$ is obtained. Thus, we can characterize the second-order topological nature of gap 1 through Q_c . For gap 2 below the Fermi level, the topological property is of the first order. Therefore, for the entire system, we can define a hybrid-order topological index $I = (Q_c, Z_2)$ to characterize the topological property.

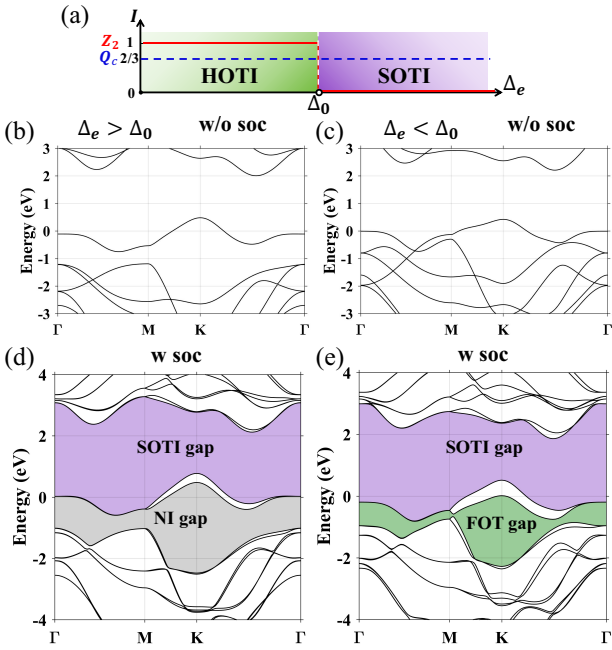


FIG. 2. (a) Diagram of hybrid-Order topological phase transition in 1H-TMCs. When Δ_e is greater than and less than Δ_0 , the band structures without SOC correspond to (b, c), respectively. The band results considering SOC are shown in (d, e), highlighting the topological features.

Using the multi-orbital TB model, we initially computed the topological properties within the two band gaps. The initial average on-site energy (E_i) difference between the d and p orbitals, denoted as $\Delta_e = \overline{E_d} - \overline{E_p}$, is greater than Δ_0 , representing the initial state of the system. Through C_3 symmetry analysis, the corner charge Q_c is calculated to be $2e/3$, and gap 1 exhibits second-order topological characteristics, marked in purple in Fig. 2 (d). On the other hand, gap 2 displays trivial insulator properties, indicated by the gray color in Fig. 2 (d). At this time, the system only exhibits second-order topological properties, with $I = (2e/3, 0)$. As Δ_e decreases, the p orbitals and d orbitals intersect along the high-symmetry line $\Gamma - M$, as shown in Fig 2 (c). Upon considering SOC, a gap opens at the merged position, and gap 2 exhibits first-order topological (FOT) features with $Z_2 = 1$, as marked in blackish green in Fig. 2 (e). At this point, the system exhibits a hybrid-order topological state, with $I = (2e/3, 1)$, displaying both second-order and first-order topological characteristics above and below the Fermi level. During the Δ_e modulation process, the critical value for the overlap of the p and d orbitals at the M point is denoted as Δ_0 . At this point, we can obtain two types of topological states near the Fermi level. Due to the constraint of the Fermi level, setting such mixed-order topological states is rare. Currently, they have only been found in TMCs. It can adjust the Fermi level position through gate voltage to enable the switching between different topological orders³³.

To determine the second-order topological features of

1H-TMCs, we construct a triangular quantum sheet using the TB model, as shown in Fig. 3 (a). The triangular flake, with a side length of 9 unit cells, exhibits six corner states within the SOTI bandgap above the Fermi level. The wave functions of the corner states are localized at the three corner positions, as illustrated in the inset of Fig. 3 (a). For the intrinsic second-order topological properties of 1H-TMCs, the surface band structure is shown in Fig. 3 (b). Two band gaps appear, one above and one below the Fermi level. Notably, the lower band gap is trivial, indicating trivial properties. However, when the system transitions to a HOTI, the band inversion occurs at the M point, and the interval of the lower band gap exhibits topological properties. The hybrid-order topological surface band structure is depicted in Fig. 3 (c). By zooming in on the local region in Fig. 3 (d), it is evident that the topological edge states connect the lower bulk band to the upper bulk band. Thus, the hybrid-order topological states achieve the bulk-edge-corner correspondence near the Fermi level.

We have not only constructed a multi-orbital TB model for 1H-TMCs, but also provide specific examples of practical materials. Materials with the potential for hybrid topological order mainly fall into two categories: metallic or semimetallic 1H-TMCs. For metals, the d orbitals cross the Fermi level, and prominent examples of HOTIs include 1H-TMCs like $NbTe/Se_2$, $TaSe_2$, and VTe/Se_2 . As for semimetals, MX_2 ($M = Cr, W, Mo$; $X = Te, S, Se$) compounds serve as candidate materials. Taking the example of the semimetal WTe_2 and the metal $NbSe_2$, we manipulate their phase transitions through tensile and compressive stresses. For WTe_2 , it exhibits intrinsic hybrid topological properties,

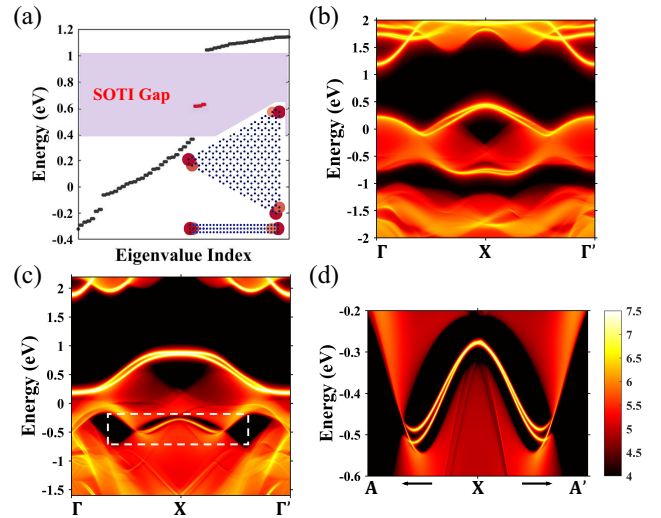


FIG. 3. (a) Energy spectrum of 1H-TMCs thin films under SOTI phase. The red dots within the SOTI bandgap represent six corner states. The localized electronic distribution of angular states occurs at the three corners. (b) Surface band corresponding to the SOTI phase. (c) Surface band structure of the HOTI phase. The local magnified view within the white dashed box is shown in (d).

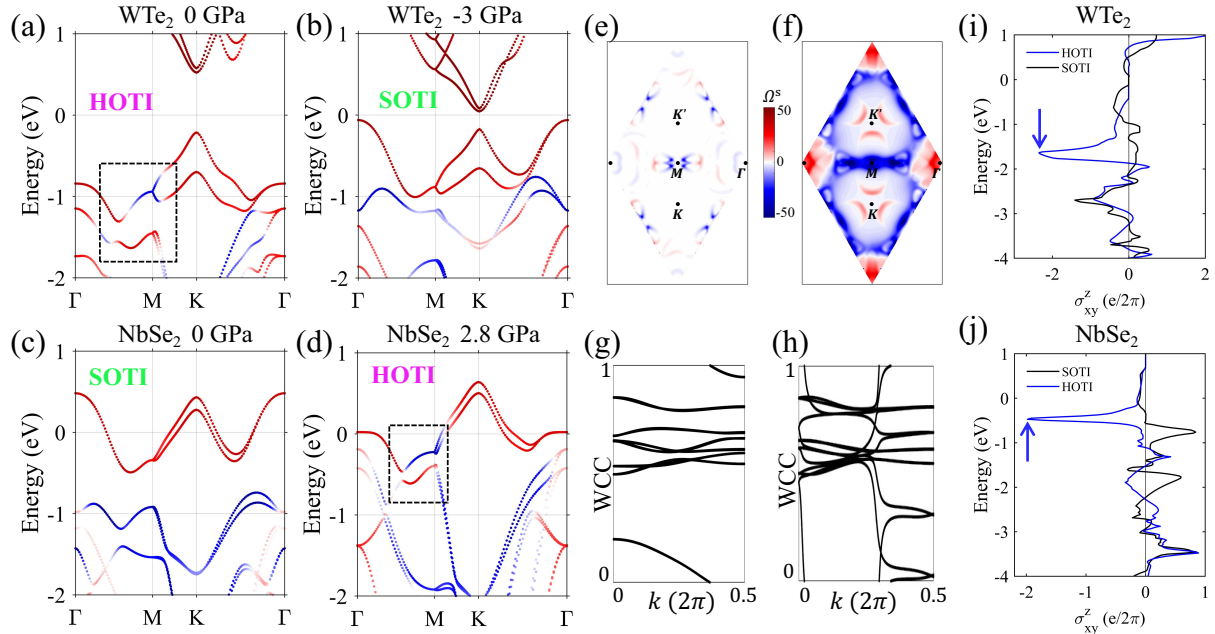


FIG. 4. (a-d) Projected band structures of WTe_2 and $NbSe_2$ under different pressures. The spin Berry curvature at the gap 2 energy level for WTe_2 is shown in (e) for SOTI and (f) for HOTI. The WCC characterization of the gap 2 region before and after the topological phase transition is shown in (g) and (h), respectively. The spin Hall conductance (SHC) in SOTI and HOTI before and after the phase transition are shown in (i) and (j), respectively, as two examples.

as shown in Fig. 4 (a), where dashed boxes mark the intervals of p and d orbital inversions. When a tensile stress of 3 GPa is applied to WTe_2 , this p , d inversion disappears, as shown in Fig. 4 (b). Meanwhile, for intrinsic $NbSe_2$, d orbital bands cross the Fermi level, with two band gap spaces above and below the orbital bands, as shown in Fig. 4 (c). Simultaneously, the calculated corner charge $Q_c = \frac{1}{3}e$ indicates the system's SOTI characteristics. When a pressure of 2.8 GPa is applied, the d and p orbitals swap positions at the high-symmetry point M, leading to band crossings along the Γ -M high-symmetry line and the opening of a gap due to SOC. This result perfectly matches the TB model, as depicted in Fig. 4 (d). Due to the first-order topological phase transition to a Z_2 topological insulator occurring in the low-energy bandgap, the topological phases before and after the transition can be distinguished by the closely related spin Berry curvature^{51,52}. Before the p , d orbitals inversion, the orbital coupling of gap 2 decreases, resulting in a small spin Berry curvature at that energy level, as shown in Fig. 4 (e). However, after the p , d inversion occurs, there is a significant enhancement in the spin Berry curvature, especially near the Γ -M high-symmetry line, as depicted in Fig. 4 (f). This change in spin Berry curvature also reveals the phase transition characteristics of Z_2 topological insulators. Based on this, by integrating the spin Berry curvature using the spin Hall conductance formula

$$\sigma_{SH} = \frac{e}{(2\pi)^2} \sum_n \int_{BZ} d^2k f_{n\vec{k}} \Omega_{n,\vec{k}}^s, \quad (3)$$

TABLE I. Hybrid-order topological materials in 1H-TMCs

Sample	HOTI	
	Intrinsic	Pressure
Semiconductor	$MoSe_2, MoTe_2$	MoS_2, WS_2
	WSe_2, WTe_2	$CrS_2, CrSe_2$
	$CrTe_2$	
Metal	$NbTe_2$	$NbSe_2, TaSe_2$
		VSe_2, VTe_2

where $\Omega_{n,\vec{k}}^s$ is spin Berry curvature. $f_{n\vec{k}}$ is Fermi distribution function. We can obtain their spin Hall conductance, as shown in Fig. 4 (i, j). It can be observed that the HOTI phase exhibits a significantly stronger SHC at the first-order topological bandgap compared to the SOTI phase. For gap 2 below the Fermi level, the Wannier charge centers (WCC) under the two different pressures are shown in Fig. 4 (g) and (h), respectively. It can be observed that before the p and d orbitals overlap at lower energy levels, gap 2 exhibits a $Z_2 = 0$. After the orbital inversion, gap 2 is characterized by $Z_2 = 1$, indicating topological properties and the system transitions to a hybrid-order topological state. Under a unified energy display standard, the differences between SOTI and HOTI are evident, primarily occurring at the Γ -M symmetry line and near the Γ point. For the hybrid-order topological candidate materials in the 1H-TMCs family, we list them in Table I. Among them, five are intrinsic hybrid-order topological materials. Additionally, six

materials exhibit HOTI topological states only under applied pressure. The DFT calculations for HOTIs in the TMCs family are presented individually in the supplementary materials⁴⁸.

Although the rule of finding different topological orders in various energy ranges, similar to phononic crystals^{2,3}, is relatively straightforward, it is extremely rare to find HOTIs like those in TMCs, where topological order switching can be achieved at the Fermi level through gate voltage regulation. The topological switchability of HOTIs breaks the limitations of conventional topological materials. Moreover, for electronic materials, only topological properties near the Fermi level are meaningful. This is the main reason why we focus our discussion on 1H-TMC, as it makes the HOTI both controllable and significant. At the same time, although the first-order topology has a non-global band gap, it exhibits a strong spin Hall effect similar to Weyl semimetals⁵³. This characteristic also demonstrates the potential of TMCs in spintronics applications.

In summary, we point out the hybrid-order topological phase and the associated phase transition process in 1H-TMCs from the perspective of multi-orbital coupling. With the help of the multi-orbital fitted TB model, we emphasize the importance of the *p* orbital at low energy in TMCs, which is crucial for the hybrid-order topological state. Meanwhile, under the influence of the crystal field effect, the hybrid-order topological phase transition in 1H-TMCs can be easily controlled. We also present the topological phase diagram of 1H-TMCs concerning the average energy difference Δ_e between the *p* and *d* orbitals. Finally, we verify the stress-controlled hybrid-order topological phase transition in the 1H semiconductor *WTe*₂ and the metal *NbSe*₂ through first-principles calculations and highlight the significant changes in spin Hall conductance and the novel bulk-edge-corner correspondence. Thus, our results not only expand the list of candidate materials for hybrid-order topology but also explore the potential interplay between orbitals and the hybrid-order topological state. Our findings pave the way for further research in hybrid-order topological physics and demonstrate its potential applications in spintronics.

We acknowledge useful discussions with Yinchuan Zhang. This work is mainly supported by the National Natural Science Foundation of China (No. 11874113) and the Natural Science Foundation of Fujian Province of China (No. 2020J02018).

The authors have no conflicts to disclose.

Ning-Jing Yang: Conceptualization (lead); Data curation (lead); Formal analysis (lead); Writing – original draft (lead). **Zhigao Huang:** Funding acquisition (lead); Project administration (equal); Resources (lead); Supervision (equal). **Jian-Min Zhang:** Project administration (lead); Resources (lead); Supervision (lead); Validation (lead); Visualization (lead); Writing – review & editing (lead).

The data that support the findings of this study are available from the corresponding authors upon reasonable request.

REFERENCES

- M. S. Hossain, F. Schindler, R. Islam, Z. Muhammad, Y.-X. Jiang, Z.-J. Cheng, Q. Zhang, T. Hou, H. Chen, M. Litskevich, *et al.*, *Nature* **628**, 527–533 (2024).
- X. Zhang, Z.-K. Lin, H.-X. Wang, Z. Xiong, Y. Tian, M.-H. Lu, Y.-F. Chen, and J.-H. Jiang, *Nat. Commun.* **11**, 65 (2020).
- Y. Yang, J. Lu, M. Yan, X. Huang, W. Deng, and Z. Liu, *Phys. Rev. Lett.* **126**, 156801 (2021).
- T. Li and H. Hu, *Nat. Commun.* **14**, 6418 (2023).
- G. Hwang and H. Obuse, *Phys. Rev. B* **108**, L121302 (2023).
- T. Mizoguchi and T. Koma, *Phys. Rev. B* **103**, 195310 (2021).
- O. Rapoport and M. Goldstein, *Phys. Rev. B* **107**, 085117 (2023).
- P. Lai, J. Wu, Z. Pu, Q. Zhou, J. Lu, H. Liu, W. Deng, H. Cheng, S. Chen, and Z. Liu, *Phys. Rev. Appl.* **21**, 044002 (2024).
- M. J. Pan, B.-X. Li, H. Wang, J. D. Liu, F. M. Chen, J. R. Huang, G. X. Qu, S. Y. Gao, B. Jiang, Y.-B. Huang, X. Shi, T.-L. Xia, H. M. Weng, and T. Qian, *Phys. Rev. B* **109**, L220102 (2024).
- S.-J. Huang, K. Park, and Y.-T. Hsu, *npj Quantum Mater.* **9**, 21 (2024).
- W. Zhao, K. Xing, L. Chen, T.-H.-Y. Vu, G. Akhgar, Y. He, A. Bake, X. Wang, and J. Karel, *Appl. Phys. Rev.* **11** (2024).
- Y. Tokura, K. Yasuda, and A. Tsukazaki, *Nat. Rev. Phys.* **1**, 126–143 (2019).
- Q. Wang, K. Huang, W. Zhao, L. Li, and X. Wang, *Appl. Phys. Lett.* **121** (2022).
- R. Córdoba and V. M. Fomin, *Appl. Phys. Lett.* **124** (2024).
- Z.-Y. Wang, X.-C. Cheng, B.-Z. Wang, J.-Y. Zhang, Y.-H. Lu, C.-R. Yi, S. Niu, Y. Deng, X.-J. Liu, S. Chen, *et al.*, *Science* **372**, 271–276 (2021).
- T. Nomoto, S. Imaio, H. Akutsu, Y. Nakazawa, and Y. Kohama, *Nat. Commun.* **14**, 2130 (2023).
- J.-M. Zhang, W. Zhu, Y. Zhang, D. Xiao, and Y. Yao, *Phys. Rev. Lett.* **109**, 266405 (2012).
- I. Levy, C. Youmans, T. A. Garcia, H. Deng, S. Alsheimer, C. Testelin, L. Krusin-Elbaum, P. Ghaemi, and M. C. Tamargo, *Nano Lett.* **20**, 3420–3426 (2020).
- E. N. Lima, T. M. Schmidt, and R. W. Nunes, *Nano Lett.* **16**, 4025–4031 (2016).
- P. Delplace, J. Li, and M. Büttiker, *Phys. Rev. Lett.* **109**, 246803 (2012).
- H. Zhang, Z. Shi, Z. Jiang, M. Yang, J. Zhang, Z. Meng, T. Hu, F. Liu, L. Cheng, Y. Xie, *et al.*, *Adv. Mater.* **35**, 2301790 (2023).
- Y. Liang, X. Han, Q. Wang, and P. Zhao, *Appl. Phys. Lett.* **124** (2024).
- A. Gao, Y.-F. Liu, C. Hu, J.-X. Qiu, C. Tzschaschel, B. Ghosh, S.-C. Ho, D. Bérubé, R. Chen, H. Sun, *et al.*, *Nature* **595**, 521–525 (2021).
- C. Bao, P. Tang, D. Sun, and S. Zhou, *Nat. Rev. Phys.* **4**, 33–48 (2022).
- M. Lohse, C. Schweizer, H. M. Price, O. Zilberberg, and I. Bloch, *Nature* **553**, 55–58 (2018).
- M. Strungaru, M. Augustin, and E. J. Santos, *npj Comput. Mater.* **8**, 169 (2022).
- B. Fu, R.-W. Zhang, X. Fan, S. Li, D.-S. Ma, and C.-C. Liu, *ACS nano* **17**, 1638–1645 (2023).
- S. Zhang, X. Dai, and J. Liu, *Phys. Rev. Lett.* **128**, 026403 (2022).
- W. Liu, Z.-K. Ding, N. Luo, J. Zeng, L.-M. Tang, and K.-Q. Chen, *Phys. Rev. B* **109**, 115422 (2024).
- J. Cheng, J. Bai, B. Ruan, P. Liu, Y. Huang, Q. Dong, Y. Huang, Y. Sun, C. Li, L. Zhang, *et al.*, *J. Am. Chem. Soc.* (2024).
- W. Li, J. Huang, X. Li, S. Zhao, J. Lu, Z. V. Han, and H. Wang, *Mater. Today Phys.* **21**, 100504 (2021).

³²L. Bawden, S. P. Cooil, F. Mazzola, J. Riley, L. Collins-McIntyre, V. Sunko, K. Hunvik, M. Leandersson, C. Polley, T. Balasubramanian, *et al.*, *Nat. Commun.* **7**, 11711 (2016).

³³J. Lu, O. Zheliuk, I. Leermakers, N. F. Yuan, U. Zeitler, K. T. Law, and J. Ye, *Science* **350**, 1353–1357 (2015).

³⁴S. Kezilebieke, M. N. Huda, V. Vaňo, M. Aapro, S. C. Ganguli, O. J. Silveira, S. Glodzik, A. S. Foster, T. Ojanen, and P. Lil-jereth, *Nature* **588**, 424–428 (2020).

³⁵S. Li, Q. Wang, C. Zhang, P. Guo, and S. A. Yang, *Phys. Rev. B* **104**, 085149 (2021).

³⁶I. Tyulnev, Á. Jiménez-Galán, J. Poborska, L. Vamos, P. S. J. Russell, F. Tani, O. Smirnova, M. Ivanov, R. E. Silva, and J. Biegert, *Nature* **628**, 746–751 (2024).

³⁷B. Sun, W. Zhao, T. Palomaki, Z. Fei, E. Runburg, P. Malinowski, X. Huang, J. Cenker, Y.-T. Cui, J.-H. Chu, *et al.*, *Nat. Phys.* **18**, 94–99 (2022).

³⁸S. Z. Uddin, N. Higashitarumizu, H. Kim, J. Yi, X. Zhang, D. Chrzan, and A. Javey, *ACS nano* **16**, 8005–8011 (2022).

³⁹X. Zhu, D. Li, R. Zhang, H. Zhang, C. Cong, M. Zhu, Y. Shi, Y. Wu, S. Wang, Y. Zheng, *et al.*, *Appl. Surf. Sci.* **519**, 146262 (2020).

⁴⁰Y. Sugita and Y. Motome, *Phys. Rev. B* **99**, 041101 (2019).

⁴¹P. Gorai, E. S. Toberer, and V. Stevanović, *Phys. Chem. Chem. Phys.* **18**, 31777–31786 (2016).

⁴²F. Pascale, K. Doll, F. S. Gentile, and R. Dovesi, *J. Comput. Chem.* **44**, 65–75 (2023).

⁴³M. Costa, B. Focassio, L. M. Canonico, T. P. Cysne, G. R. Schleder, R. B. Muniz, A. Fazzio, and T. G. Rappoport, *Phys. Rev. Lett.* **130**, 116204 (2023).

⁴⁴G. Long, M. Pan, H. Zeng, and H. Huang, *Phys. Rev. Mater.* **8**, 044203 (2024).

⁴⁵J. Kang, X. Qiu, Q. Hu, J. Zhong, X. Gao, R. Huang, C. Wan, L.-M. Liu, X. Duan, and L. Guo, *Nat. Catal.* **4**, 1050–1058 (2021).

⁴⁶S. V. Streltsov, A. S. Mylnikova, A. O. Shorikov, Z. V. Pchelkina, D. I. Khomskii, and V. I. Anisimov, *Phys. Rev. B* **71**, 245114 (2005).

⁴⁷H.-J. Tan, H.-H. Zhang, X.-B. Li, Y. Xu, X.-L. Wei, W.-J. Yin, and L.-M. Liu, *J. Phys. Chem. Lett.* **13**, 9287–9294 (2022).

⁴⁸“See supplemental material for (I) computational details, (II) tight-binding model, (III) shc of hybrid-order topological phase, (IV) hybrid-order topological materials in semiconductors, (V) hybrid-order topological materials in metals.”

⁴⁹W. A. Benalcazar, B. A. Bernevig, and T. L. Hughes, *Phys. Rev. B* **96**, 245115 (2017).

⁵⁰W. A. Benalcazar, T. Li, and T. L. Hughes, *Phys. Rev. B* **99**, 245151 (2019).

⁵¹P. Giannozzi, S. Baroni, N. Bonini, *et al.*, *J. phys.-Condens. Mat.* **21**, 395502 (2009).

⁵²F. T. Cerasoli, A. R. Supka, A. Jayaraj, M. Costa, I. Siloi, J. Ślawińska, S. Curtarolo, M. Fornari, D. Ceresoli, and M. B. Nardelli, *Comp. Mater. Sci.* **200**, 110828 (2021).

⁵³S. Shi, S. Liang, Z. Zhu, K. Cai, S. D. Pollard, Y. Wang, J. Wang, Q. Wang, P. He, J. Yu, *et al.*, *Nat. Nanotechnol.* **14**, 945–949 (2019).